



# Solar System Objects Observed with *TESS*—First Data Release: Bright Main-belt and Trojan Asteroids from the Southern Survey

András Pál<sup>1,2,3</sup> , Róbert Szakáts<sup>1</sup> , Csaba Kiss<sup>1</sup> , Attila Bódi<sup>1,4</sup> , Zsófia Bognár<sup>1,4</sup> , Csilla Kalup<sup>1,2</sup>, László L. Kiss<sup>1</sup> , Gábor Marton<sup>1</sup> , László Molnár<sup>1,4</sup> , Emese Plachy<sup>1,4</sup> , Krisztián Sárneczky<sup>1</sup> , Gyula M. Szabó<sup>5,6</sup> , and Róbert Szabó<sup>1,4</sup> 

<sup>1</sup>Konkoly Observatory, Research Centre for Astronomy and Earth Sciences, H-1121 Budapest, Konkoly Thege Miklós út 15-17, Hungary; [apal@szofi.net](mailto:apal@szofi.net)

<sup>2</sup>Eötvös Loránd University, H-1117 Pázmány Péter sétány 1/A, Budapest, Hungary

<sup>3</sup>MIT Kavli Institute for Astrophysics and Space Research, 70 Vassar Street, Cambridge, MA 02109, USA

<sup>4</sup>MTA CSFK Lendület Near-Field Cosmology Research Group, Konkoly Observatory, Budapest, Hungary

<sup>5</sup>ELTE Eötvös Loránd University, Gothard Astrophysical Observatory, Szombathely, Hungary

<sup>6</sup>MTA-ELTE Exoplanet Research Group, 9700 Szombathely, Szent Imre h. u. 112, Hungary

Received 2019 October 30; revised 2019 December 9; accepted 2019 December 11; published 2020 March 5

## Abstract

Compared with previous space-borne surveys, the *Transiting Exoplanet Survey Satellite* (*TESS*) provides a unique and new approach to observe solar system objects. While its primary mission avoids the vicinity of the ecliptic plane by approximately six degrees, the scale height of the solar system debris disk is large enough to place various small body populations in the field of view. In this paper we present the first data release of photometric analysis of *TESS* observations of small solar system bodies, focusing on the bright end of the observed main-belt asteroid and Jovian Trojan populations. This data release, named TSSYS-DR1, contains 9912 light curves obtained and extracted in a homogeneous manner, and triples the number of bodies with unambiguous fundamental rotation characteristics, namely where accurate periods and amplitudes are both reported. Our catalog clearly shows that the number of bodies with long rotation periods are definitely underestimated by all previous ground-based surveys, by at least an order of magnitude.

*Unified Astronomy Thesaurus concepts:* [Period search \(1955\)](#); [Observational astronomy \(1145\)](#); [Main belt asteroids \(2036\)](#); [Jupiter trojans \(874\)](#); [CCD photometry \(208\)](#); [Time series analysis \(1916\)](#)

## 1. Introduction

The *Transiting Exoplanet Survey Satellite* (*TESS*; Ricker et al. 2015) was successfully launched on 2018 April 18 and after commissioning, started its routine operations on 2018 July 25. During the first two years of its primary mission, *TESS* observations are scheduled in terms of “*TESS* sectors” (or simply, sectors) where each sector corresponds to roughly 27 days of nearly continuous observations (in accordance with two orbits of *TESS* around Earth, with a spacecraft orbit in 1:2 mean-motion resonance with the Moon). The first year of observations ended on 2019 July 18, after completing the 13th sector (S13). Throughout these 13 sectors, *TESS* observed the primary fields on the southern ecliptic hemisphere, covering the sky from the ecliptic latitude of  $\beta \approx -6^\circ$ , down to the southern ecliptic pole.<sup>7</sup> This coverage is attained by four wide-field cameras, each camera having a field of view (FoV) of  $24^\circ \times 24^\circ$ , and the gross FoV is equivalent to a nearly contiguous rectangle in the sky, with a size of  $96^\circ \times 24^\circ$ . The individual camera FoVs are also identified by the camera numbers and, according to the survey design, Camera #4 continuously stared at the southern ecliptic pole while Camera #1 scanned the subsequent fields just south from the ecliptic plane. The cadence of *TESS* observations is 30 minutes in the so-called full-frame image (FFI) mode while preselected sources are observed with a cadence of 2 minutes (hence, this mode is also called the “postage stamp” mode). These two modes are also referred to as *long cadence* and *short cadence* observations: for *TESS*, long cadence also implies that the whole CCD frame is retrieved.

This mission design allows us to observe solar system objects during the primary mission, even considering the fact that the ecliptic plane is avoided by  $\sim 6^\circ$ . At first glance, objects with an inclination higher than  $\sim 6^\circ$  are expected to be observed, but due to the  $\sim 1$  au distance of *TESS* to the Sun and the semimajor axis range of 2.1–3.3 au for the main-belt asteroids, also considering their nonzero eccentricities, thousands of objects with a few degrees of inclination are also possible to be observed with the aforementioned spacecraft attitude configuration. This limit of  $6^\circ \lesssim i$  is more strict for distant objects, such as Centaurs or trans-Neptunian objects.

According to earlier simulations (Pál et al. 2018), one can expect good quality photometry of moving targets down to  $V \lesssim 19$  mag with a time resolution of 30 minutes corresponding to the data acquisition cycle of the *TESS* cameras in full-frame mode. Although the cadence for the postage stamp mode frames would allow a similar precision down to the brighter objects (i.e.,  $V \lesssim 16$  mag), the corresponding pixel allocation would be too expensive. In this aspect, *TESS* short cadence observations are analogous to the *Kepler/K2* mission (Borucki et al. 2010; Howell et al. 2014), and similarly, only preselected objects could be observed in this mode (Pál et al. 2015; Szabó et al. 2015). Specifically, one should allocate roughly a thousand pixel-wise stamp if observations for a certain object are required. The rule of thumb for the apparent tracks of main-belt asteroids on long cadence *TESS* images is the movement of  $\approx 1$  pixel/cadence (see also Figure 2 in Pál et al. 2018). Of course, near-Earth objects and trans-Neptunian objects could have apparent speeds that are larger and smaller, respectively.

The yield of such a survey performed by *TESS* is a series of (nearly) uninterrupted, long-coverage light curves of solar

<sup>7</sup> <https://tess.mit.edu/observations/>

system objects—like in the case of the previous space-borne studies mentioned below. From these light curves, one can obtain fundamental physical characteristics of the bodies such as rotation periods, shape constraints, and signs of rotating on a non-principal axis—with a much lesser ambiguity than in the case of ground-based surveys. This ambiguity is mainly due to the fact that ground-based photometric data acquisition is interrupted by diurnal variations—which yield not just stronger frequency aliasing but higher fraction of long-term instrumental systematics. In addition, the knowledge of rotation period helps to resolve the ambiguity of rotation and thermal inertia (see e.g., Delbo et al. 2015) in thermal emission measurements of small bodies. Further combination of spin information with thermal data (see, e.g., Müller et al. 2009; Szakáts et al. 2017; Kiss et al. 2019)<sup>8</sup> can therefore be an important initiative.

This paper describes the first data release, TSSYS-DR1, of the *TESS* minor planet observations, based on the publicly available *TESS* FFI data for the first full year of operations on the southern hemisphere. The structure of this paper is as follows. In Section 2 we describe how the objects were identified and what kind of object selection principles are available for a mission like *TESS*. In Section 3 we discuss the main steps of the data reduction and photometry, emphasizing the importance of differential image analysis. Section 4 summarizes the structure of the available data products, while in Section 5 we make a series of comparisons with existing databases aiming to collect photometric data series for small solar system bodies. Our findings are summarized in Section 6.

## 2. Object Selection

Regarding the identification and querying solar system objects on *TESS* FFIs, one can ask two types of questions:

1. When and by which camera/CCD was my target of interest observed?
2. Which objects were observed by a certain camera/CCD during a given sector?

We can also connect these questions to the *K2* solar system observations. Namely, the first question is related to the computation of the pixel coverage of an asteroid track, as it was done in the case of the *K2* mission while observing preselected objects (see, e.g., Pál et al. 2015, 2016; Kiss et al. 2016), and the second question is related to the observations of serendipitous asteroids crossing large, contiguous *K2* super-stamps (Szabó et al. 2016; Molnár et al. 2018).

In order to identify the objects that were observed by a certain camera/CCD during a given sector, we followed a similar approach as was done in our *K2* asteroid studies (Szabó et al. 2016; Molnár et al. 2018) and in the case of simulations of *TESS* observations (Pál et al. 2018). Our solutions are based on an off-line tool called EPHEMD, providing a server-side backend for massive queries optimized for defining longer time intervals and larger FoVs within the same call (see Pál et al. 2018 for more details). In fact, the catalog presented in this paper is retrieved by simply executing EPHEMD queries on a per-CCD basis for each sector. Due to the dramatic decrease of the asteroid density at higher ecliptic latitudes, in this catalog (DR1) we included only the observations from Camera #1.

## 3. Data Reduction and Photometry

As was mentioned above, the whole data processing of this catalog was based on the observations performed by Camera #1 while surveying *TESS* sectors ranging from 1 up to 13. The processing has been carried out on a per-CCD basis, executing the same set of routines on the  $13 \times 4 = 52$  blocks of images corresponding to a single-sector-single-CCD acquisition run. The pipeline providing the light curves is exclusively based on the FITSH package (Pál 2012). In this section we summarize the main steps of the photometric processing.

### 3.1. CCD-level Steps

Each of the CCD image series is processed as follows. Based on the available orbital and pointing data, we selected nearly a dozen frames called individual median reference frames (IMRFs) spanning a  $\sim 2$  day long period interval close to the center of the observations evenly. These frames coincide for all four of the CCDs for a given sector, i.e., these correspond to the same cadence and usually have a time step of 4 hr between each frame. Another set of criteria was based on the constraint that both the Sun and the Moon should have been below the sunshade of the spacecraft, meaning that both the Sun–*TESS*–boresight and the Moon–*TESS*–boresight angles should have been larger than  $90^\circ$ . This combined selection criteria ensured the lack of stray light in *all* of the cameras at the same time, while the duration ensured an expected coverage of several tens of pixels of a main-belt asteroid while still keeping the differential velocity aberration at a considerably low level. In addition to the aforementioned selection criteria, if a prospective frame was flagged with a “reaction wheel desaturation event” (see Tenenbaum & Jenkins 2018), the next or previous frame was selected instead.

In the next step, IMRFs were used to create a median image, employed as a median differential background reference image (MDBRI). This MDBRI was then subtracted from all of the images acquired by the same CCD in the same sector and the resulting differences were smoothed using a median window filtering combined with spline interpolation with a grid size of  $64 \times 64$  pixels. This step allowed the derivation of large-scale background variations and nicely helped to minimize and model the variations inducted by scattered light and zodiacal light. The derived background variations were then subtracted from all of the images and image convolution was applied between the MDBRI and these background-subtracted images. Note that this step does not subtract the *intrinsic* background since such a background practically does not exist for *TESS* images due to the very strong confusion and large pixel size. The image convolution steps correct not only for the point-spread function (PSF) variations but for the offsets inducted by the differential velocity aberration as well. The latter one can be as large as one-tenth of a pixel throughout a sector and it is most prominent farther away from the spacecraft boresight (which includes Camera #1, CCDs #3 and #4, which are the closest to the ecliptic plane). Once the convolved MDBRIs are derived, the resulting residual image was processed by a spline-smoothed median window filtering with a block size of  $1 \times 64$  pixels. This filtering removed the vertical stripes exposed in the *TESS* CCDs in parallel with the increased stray light. The steps of the aforementioned processing are displayed in Figure 1 via the example of (2429) Schurer.

<sup>8</sup> [https://ird.konkoly.hu/data/SBNAF\\_IRDB\\_public\\_release\\_note\\_2019March29.pdf](https://ird.konkoly.hu/data/SBNAF_IRDB_public_release_note_2019March29.pdf)

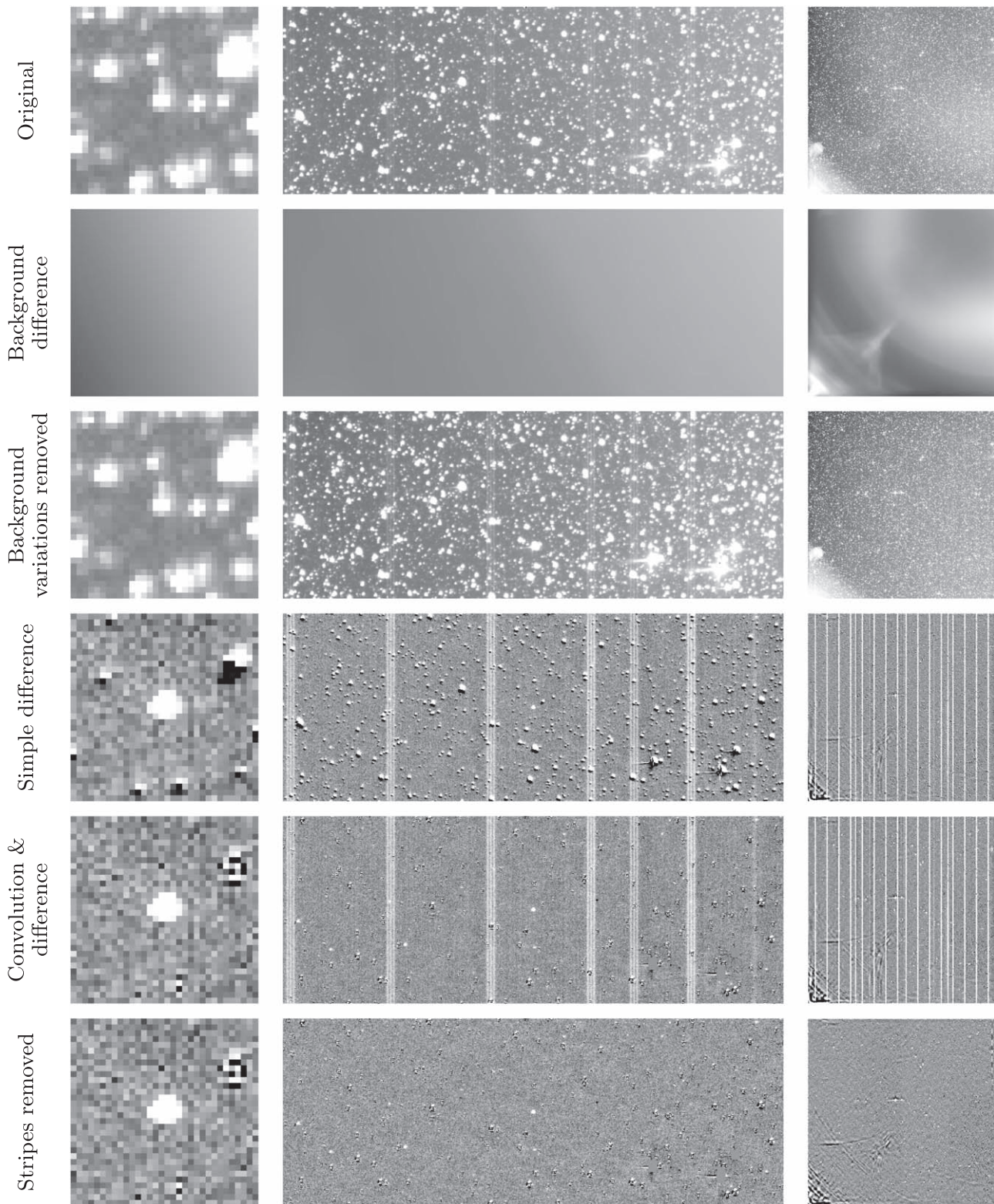


**Figure 1.** Panels showing the various stages of the image-level data processing using asteroid (2429) Schurer as an example, observed during Sector 2, by Camera #1, CCD #3. The left column shows the  $10' \times 10'$  vicinity of the target, the middle column shows the neighborhood ( $3.7 \times 1.4^\circ$ ) area, while the right column is the full CCD frame, all at the *TESS* FFI cadence 2018247095941 (JD 2458365.92767). Images in the first row show the original unprocessed data. The second row is the difference in the background structure with respect to a frame where the Earth and Moon were below the sunshade of *TESS*. The large-scale variations due to the stray light are clearly visible. The third row shows the difference between the first two rows. The fourth row shows the naive difference between the target image and the MDBRI. The residuals due to the uncorrected differential velocity aberration are clearly visible. The fifth row shows the results of the image convolution followed by subtraction. This step also makes the *TESS*-specific, but otherwise comparatively faint, vertical CCD stripes visible. In addition, the left stamp in this row shows that the sources, even ones brighter than the target objects are completely removed, with some residual structure only visible at a much brighter star at the top right corner of this stamp. Images in the sixth row show the results of the stripe removal process. The target at the center is clearly visible.

**Table 1**  
Quality Flags and Bits for the Individual Light-curve Data Points

Bit Position	Value	Description
0	1	Attitude Tweak.
1	2	(Safe Mode.)
2	4	Spacecraft is in Coarse Point.
3	8	Spacecraft is in Earth Point.
4	16	Argabrightening event.
5	32	Reaction Wheel desaturation Event.
6	64	(Cosmic Ray in Optimal Aperture pixel).
7	128	Manual Exclude. The cadence was excluded because of an anomaly.
8	256	(Discontinuity corrected between this cadence and the following one.)
9	512	(Impulsive outlier removed before cotrending.)
10	1024	Cosmic ray detected on collateral pixel row or column.
11	2048	Stray light from Earth or Moon in camera FOV.
12	4096	Formal photometric noise exceeds the threshold of 0.5 magnitude.
13	8192	Point rejected due to the presence of unexpected histogram region.
14	16,384	Manual removal of an outlier point.

**Note.** The data point flags are interpreted in a bitwise logical or combination of these individual flags. The bit positions between 0 and 11 (values from 1 to 2048) are inherited from the FITS headers of the calibrated FFI data products, in accordance with the *TESS* Science Data Products Description Document (Tenenbaum & Jenkins 2018). The bit positions from 12 to 14 (mask values from 4096 to 16,384) are specific for this particular data release and might be altered in the future. Note that bits at positions 1, 6, 8, and 9 (having a description in parentheses) are not used in the *TESS* FFI data products.

### 3.2. Target Astrometry and Photometry

These cleared images were then used as the input of the aperture photometry where the centroids are computed by the EPHEMD tool with *TESS* set as the observer’s location. Absolute astrometric plate solutions have been derived using the *Gaia* DR2 catalog (Gaia Collaboration et al. 2016, 2018), while the projection function was obtained by a third-order Brown–Conrady model on the top of tangential projection with additional refinements using a third-order polynomial expansion. The fluxes are extracted using the proper way needed to interpret convolved differential images (see Equation (83) in Pál 2009). The zero-point of the light curves was obtained using a global fit against the GAIA DR2 RP magnitudes. Due to the almost perfect overlap of the *TESS* and GAIA RP passbands—see also Figure 1 in Ricker et al. (2015) and Figure 3 in Jordi et al. (2010)—this yields a good and accurate match of the zero-point. However, offsets can be presented due to the PSF variations across the FoV of the fast *TESS* optics. We note here that the formal uncertainties do not include the respective uncertainty of this offset. Individual light-curve files were then generated by transposing the photometric results and flagged afterward according to the quality flags presented in the *TESS* FFI headers (Tenenbaum & Jenkins 2018). Light curves with an insufficient number of data points were removed from the database and the post-filtering of these remaining light curves also added additional types of quality flags (see Table 1). This post-filtering process includes exclusion of the points with high formal photometric uncertainty, outlier detection based on

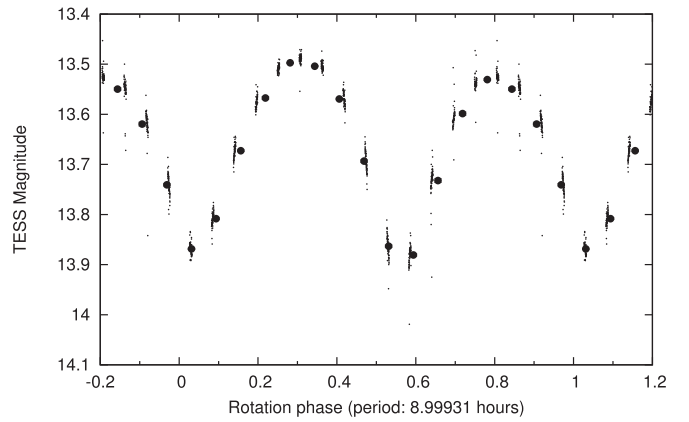


**Figure 2.** Folded light curve of (692) Hippodamia, having a rotation period  $P = 8.9993$  hr. While this rotation period satisfies the Nyquist criterion, the phase coverage is not uniform due to the  $P/C$  ratio of  $\sim 18$ .

histogram clipping, and manual removal of points in the most prominent cases.

The filtered light curves were then analyzed by performing a period search. This period search was based on fitting a sinusoidal variation in parallel with the decorrelation of the phase angle variations up to the second order (see also Section 4.2). The most dominant frequency was computed by interpolating in the vicinity of the frequency spectrum were the rms of the aforementioned fit residual was found to be the smallest (see Section 4.2). The light curves were then folded and binned after phase angle correction. Folding was performed with two periods, one corresponding to the dominant frequency, while the other period we used was twice the dominant period, assuming a double-peaked light curve generated by the rotation of an elongated body.

In total, 9912 objects are included in the present data release, for which accurate light-curve information was derived with a reasonable significance. Out of these 9912 objects, 125 have only provisional designations and therefore are not numbered minor planets.

### 3.3. Sampling Characteristics

The observing strategy of *TESS* is highly deterministic compared to many of the surveys and ground-based observations. Namely, the cadence is strictly  $C = 0.5$  hr for a nearly uninterrupted observing period of  $L \lesssim 25$ –28 days. This property implies the Nyquist criterion that does not allow the unambiguous rotation characterization for objects having a period of  $P \leq 2C = 1$  hr. This is interesting for small objects, having a size of approximately or smaller than the spin barrier limit of  $\sim 100$  m: such objects can rotate faster than  $\sim 2.2$  hr (Pravec & Harris 2000).

The strict cadence also yields sampling artifacts of objects having a rotation period that is close to the integer multiple of the cadence  $C$ . For instance, (692) Hippodamia has a rotation period of  $P = 8.9993$  hr, which is almost exactly 18 times longer than the *TESS* FFI cadence (see Figure 2). In order to characterize the strength of this sampling effect, let us assume that the period of the object is  $P = nC + \varepsilon$  where  $\varepsilon$  represent a short time difference and  $n$  is an integer number (e.g.,  $n = 18$  and  $\varepsilon = -0.0007$  hr for (692) Hippodamia). In order to fully sample the rotational phase domain, one should expect that the second instance ( $t = C$ ) has the same phase as the last phase after, at, or around the  $k$ th rotation where for the total

observation the time span is  $L \approx kP$ . Here  $k$  is also an integer, the total number of rotations covered during the observations. The phases are equal if  $(knC/P) - (C/P) = k$ , from which we can compute that  $CP/L$  should be smaller than  $|\varepsilon|$ . This limit for (692) Hippodamia is  $|\varepsilon|_{692} = (1/2 \text{ hr}) \cdot (8.9993 \text{ hr}) / (25 \text{ days}) \approx 0.0075 \text{ hr}$ , definitely larger than  $|\varepsilon| = 0.0007 \text{ hr}$ , which we obtained above for this object, resulting in a stroboscopic effect. This stroboscopic effect is also present in  $K2$  observations; see, e.g., the case of (14791) Atreus in Szabó et al. (2017).

#### 4. Database Products and Structures

Per-object data products were saved and stored in accordance with the aforementioned steps. The primary data products include four files per object, namely:

1. the light-curve file, containing the time series of the brightness measurements for a particular object;
2. the residual rms frequency spectrum;
3. a metadata file (best-fit rotation frequency, peak-to-peak amplitude, light-curve type);
4. validation sheets, including the plots of the aforementioned data products; and
5. per-object summary plots and slides, including the folded light curve with the most likely rotation period.

In the following, we describe these data products in more detail. The full data release is available at <https://archive.konkoly.hu/pub/tssys/dr1/>.

##### 4.1. Light-curve Files

The light-curve files basically represent the post-transposition stage of the photometric output. Since photometry is performed on a per-frame basis and a single call to the photometric task (FITSH/fiphot) performs the flux extraction for all of the minor planets associated with that particular frame, light-curve files also include the target name, the timestamp, the  $(x, y)$  pixel coordinates, and estimations for the background structure. Although differential imaging analysis and the subsequent photometry yield zero local background on subtracted images in theory, some artifacts—such as stray light spikes, unmasked blooming, prominent residual structures around bright but unsaturated stars—cause deviations from the zero level. Such information is therefore useful for further filtering of outliers and associating quality flags to the photometric data points. In addition to the aforementioned data, light-curve files are extended with three additional columns showing the phase angle values, observer-centric distances, and heliocentric distances.

##### 4.2. Residual Spectra

Residual spectra are generated by frequency scanning with a step size and coverage in accordance with the *TESS* sector time span and the *TESS* FFI cadence, respectively. Namely, the total time span of  $\sim 27$  days on average implies a step size of  $\Delta f = 0.01 \text{ c day}^{-1}$ , while the Nyquist criterion maximizes the scanning interval in  $f_{\text{max}} = 24 \text{ c day}^{-1}$ . The residual spectrum is then computed for a certain input frequency  $f$  by minimizing

the parameters  $A$ ,  $B$ , and  $k_i$  ( $i = 0, 1, 2$ ) for the model function

$$m(t) = \sum_{i=0}^2 k_i [\alpha(t) - \alpha_0]^i + A \cos[2\pi f(t - T_0)] + B \sin[2\pi f(t - T_0)], \quad (1)$$

where  $m(t)$  is the observed magnitude (corrected for the variations in the solar and observer distances) at the instance  $t$ ,  $\alpha$  is the phase angle,  $\alpha_0$  is the mean phase angle throughout the observations, and  $T_0$  is an approximate mid-time of the observations. The actual values of  $\alpha_0$  and  $T_0$  do not alter the residuals (hence the spectra); however, setting the aforementioned values helps to minimize the numerical round-off errors and  $k_0$  can also be interpreted as a mean brightness magnitude throughout the observations.

##### 4.3. Metadata

In the case of the light-curve and residual spectrum analysis, metadata represents the rotation frequency (and/or, equivalently, the rotation period), the characteristics of the light-curve shape, and the peak-to-peak amplitude as well as any associated external database. While the processing scripts store metadata in separate files in a form of key-value pairs, the final data product includes a list of concatenated metadata in a tabular form.

In addition, this metadata table is extended with various large asteroid database information for convenience and further analysis. This information can be used to create additional types of statistics and have estimations for biases (see Section 5 for examples). In our published database, we included the most recent version of the synthetic proper orbital elements of Knežević & Milani (2000), as available online,<sup>9</sup> the asteroid family catalog Version 3 of Nesvorný et al. (2015), and the most recent version of the Asteroid Lightcurve Database (LCDB; Warner et al. 2009). Of course, the overlap with either of the aforementioned databases is incomplete, and there are only 1563 objects for which both proper orbital elements and LCDB data are available.

##### 4.4. Validation Plots

For a quick manual vetting of the results of the photometric analysis, we create a four-panel summary plot for each object. The four plots are the unfolded light curve, the residual spectrum, the folded light curve with the dominant period, and the folded light curve with the double of the dominant period.

##### 4.5. Object Light-curve Plots and Slides

These plots contain the same information as the validation plots, but in a bit different arrangement, and these display only a single folded light curve with the most likely rotation period. The plots also show this rotation period in the units of hours. We note here that the time instances for both the plots and all of the light-curve data products are given in Julian Days. As an example, two of such object light-curve plots are displayed in Figure 3 for the objects (354) Eleonora and (220281) 2003 BA<sub>47</sub>. These objects represent the bright end and the faint end of our catalog.

<sup>9</sup> <https://newton.spacedys.com/astdys2/>

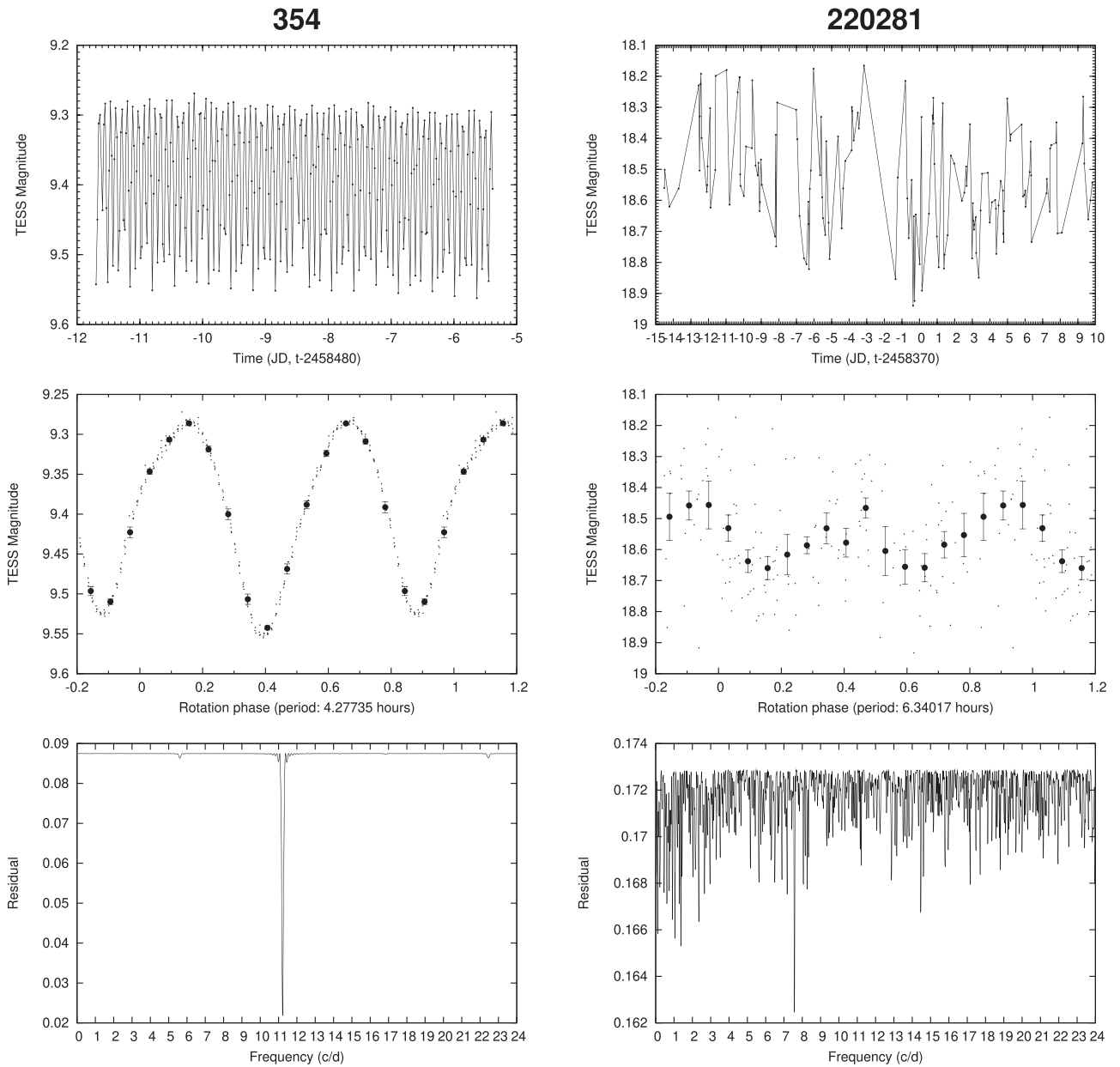


**Figure 3.** Object light-curve plots for (354) Eleonora (left column) and (220281) 2003 BA<sub>47</sub> (right column). These plots are available for all of the 9912 objects presented in this study.

## 5. Comparison with Existing Databases

### 5.1. Asteroid Lightcurve Database—LCDB

The most comprehensive database available in the literature is the Asteroid LCDB<sup>10</sup> (see Warner et al. 2009). The most recent (2019 August) release of this database contains 4842 objects for which a valid rotation period *and* brightness variation amplitude are associated.<sup>11</sup> While this amount of data is nearly half of the entries available in the *TESS* minor planet data, the LCDB cites 2788 bibliographic sources (concerning the entire database); therefore, one should consider the inhomogeneity while interpreting LCDB statistics. However, we expect that the aforementioned quality constraints of

selecting 4842 objects ensure the robustness of the data products.

In total, we identified 624 objects that are available both in TSSYS-DR1 and LCDB (with sufficiently strong qualification). We note here that there are 1535 objects available both in TSSYS-DR1 and LCDB if we do not consider the amplitude quality criteria mentioned above. In Figures 4 and 5 we displayed the rotation frequency and amplitude correlations, respectively, between the two databases. Considering the rotation periods, we found that the agreement is perfect for  $\sim 80\%$  of the objects, while there are a few dozens of objects where the double-peaked ambiguity yields a 1:2 or 2:1 ratio. The amount of such ambiguities is roughly the same (19 versus 28) for the two ratios. Otherwise, it is worth mentioning here that *TESS* clearly identifies the objects with longer periods better, suspecting an unclear origin of the otherwise shorter reported periodicity in LCDB (see the points above the 1:1 and

<sup>10</sup> <http://www.minorplanet.info/lightcurvedatabase.html>

<sup>11</sup> We note here that incomplete amplitude information but settled rotation periods are available for 20,462 objects.

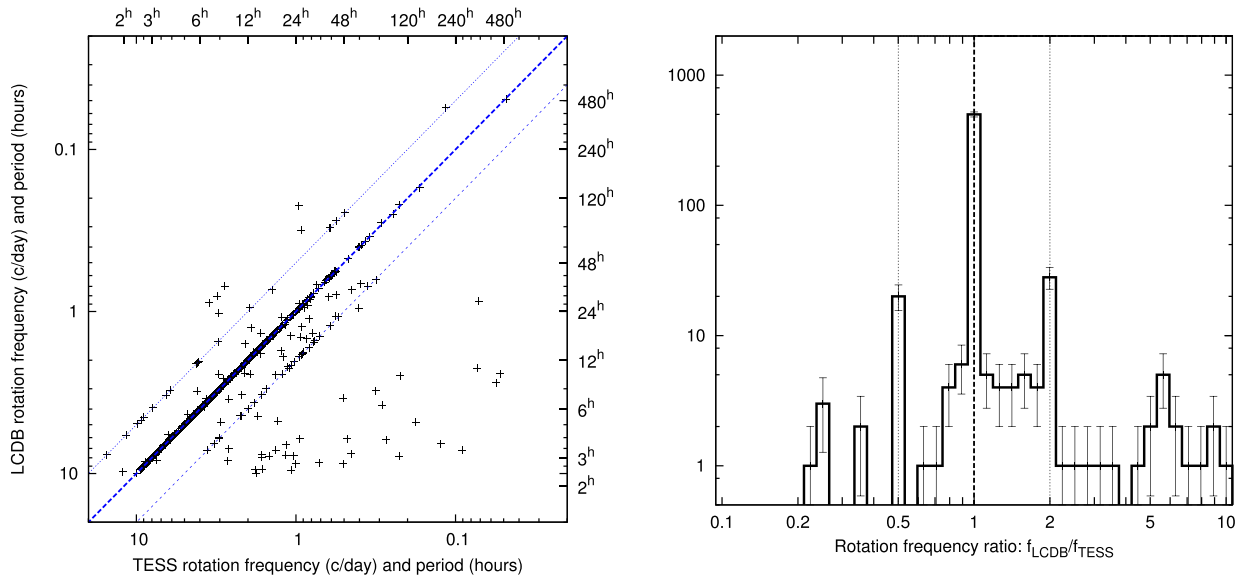


**Figure 4.** Left panel shows the rotation periods of the 624 objects for which reliable rotation characteristics (i.e., periods and amplitudes) are available both in the LCDB catalog and the *TESS* observations presented in this paper. The thick line and the two dashed lines correspond to the same rotation frequencies as well as the 1:2 and 2:1 ratios, respectively. Right panel displays the histogram of the frequency ratios of the objects available both in the LCDB catalog and the presented *TESS* minor planet catalog. In total,  $\sim 80\%$  of the matched objects have the same derived rotation periods, while in the case of  $\sim 8\%$  of the objects, the newly derived preferred periods are either double or half of the periods available in the LCDB. *TESS* measurements clearly identified longer rotation periods for the majority of the remaining  $\sim 60$  objects.

2:1 line in the left panel of Figure 4 or the histogram distribution at the right tail in the right panel of Figure 4).

Regarding the interpretation of the correlations between amplitudes (see Figure 5), the larger amplitudes present in the LCDB are a clear signature of the bias in the *TESS* observations. Namely, *TESS* observes minor planets close to the opposition, i.e., at small phase angles, while LCDB contains many kinds of observations (yielding better coverage in phase angles), not just ones close to the opposition. According to the expectations (Zappala et al. 1990), higher phase angles would yield higher amplitudes, which can explain the shift in the correlation diagram and the corresponding histogram. However, one should note that because of this *TESS*-specific observing constraint as well as due to the fact that the presented data release contains only a single epoch while LCDB aggregates data from many observing runs, such a statistical comparison between *TESS* and LCDB amplitudes needs to be considered tentative. While the presented *TESS* data series is highly homogeneous, it shows amplitude characteristics only for a single observing geometry, leaving many aspects of shape characteristics ambiguous.

### 5.2. *K2* Solar System Studies—*K2SSS*

While having scanned various fields close to the ecliptic plane, the *K2* mission (Howell et al. 2014) also provided a highly efficient way to provide uninterrupted observations for various classes of solar system objects. These classes include not only main-belt and Trojan asteroids but trans-Neptunian objects (Pál et al. 2015), irregular satellites of giant planets (Kiss et al. 2016; Farkas-Takács et al. 2017), and the Pluto–Charon system (Benecchi et al. 2018). *K2* observations also implied the discovery of the satellite of (225088) 2007 OR<sub>10</sub> (Kiss et al. 2017) when its slow rotation was detected (Pál et al. 2016).

With the exception of the discovery and photometry of the trans-Neptunian object (506121) 2016 BP<sub>81</sub> (Barentsen et al.

2017), all of these object classes were measured as targeted observations, i.e., with pre-allocated *K2* target pixel files (arranged into special boomerang-shaped pixel blocks). In the case of main-belt and Trojan asteroids, there are examples of targeted observations (Ryan et al. 2017; Szabó et al. 2017; Marciniak et al. 2019) as well as photometry on contiguous superstamps (Szabó et al. 2016; Molnár et al. 2018) when asteroids serendipitously crossed these celestial areas. However, the data reduction pattern does not differ significantly for pre-allocated reductions and the analysis of contiguous superstamps with the exception of the aforementioned querying of the objects (by tools like EPHEMD) in the latter case. See, e.g., Szabó et al. 2017 for a detailed description about the data reduction for *K2* minor planet observations observations.

In order to compare the objects observed by any initiative of the *K2* solar system surveys with this recent *TESS*-based photometry, we identified six main-belt and Trojan objects that were observed both by *K2* and *TESS*. These were (24534) 2001 CX<sub>27</sub>, (24537) 2001 CB<sub>35</sub>, (37750) 1997 BZ, (42573) 1997 AN<sub>1</sub>, (45086) 1999 XE<sub>46</sub>, and (65210) Stichius. We found that the derived rotation periods match perfectly in five of the six cases; see Figure 6. There was only a slight offset for (65210) Stichius, due to its faintness and long rotation period of  $\sim 32$  hr.

### 5.3. Period Statistics

In Figure 7 we displayed the histograms of the detected rotation periods for this *TESS*-based asteroid survey, the LCDB and the *K2* serendipitous main-belt asteroid detections on the M35 and Neptune–Nereid fields (Szabó et al. 2016), as well as on the Uranus field (Molnár et al. 2018). A tentative fit in the long-period part of these histograms clearly shows that both ground-based and shorter duration but otherwise uninterrupted space-borne measurements underestimate the number of objects in the population of slow rotators. Therefore, we can safely conclude that the nearly one-month-long continuous data

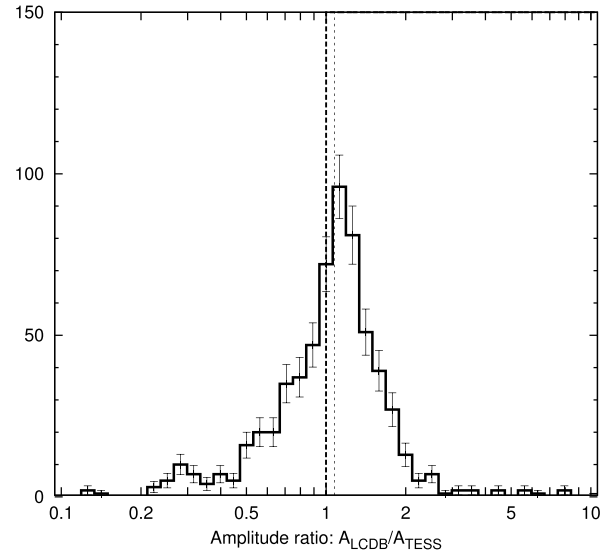
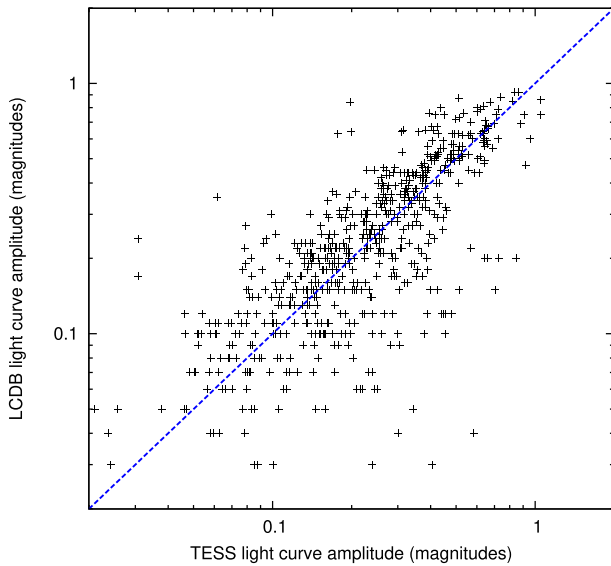


**Figure 5.** Left panel: light-curve peak-to-peak amplitudes for the 624 objects where rotation characteristics are available both in the LCDB catalog and the *TESS* observations presented here. Right panel: the histogram of the distribution of the amplitude ratios. The thick vertical line shows the unity ratio, while the thin vertical dashed line at  $\sim 1.076$  shows the median value of the amplitude ratios.

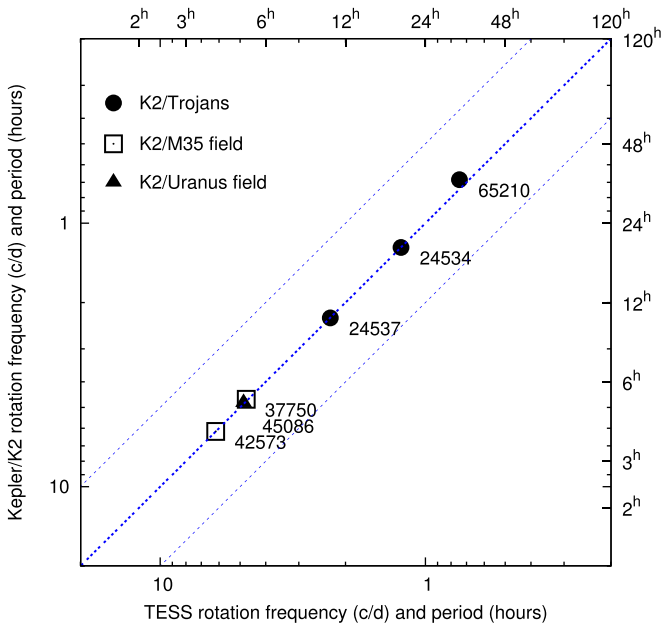


**Figure 6.** Six minor planets for which both *Kepler/K2* and *TESS* measurements are available. Three out of these six objects are Jupiter Trojans, while the another two are main-belt asteroids. With the exception of the Trojan asteroid (65210) *Stichius*, the periods match within 1.5%. The agreement for (24534) 2001 CX<sub>27</sub> and (42573) 1997 AN<sub>1</sub> are less than one-tenth of a percent. (65210) *Stichius* shows a difference of  $\sim 8\%$  between the derived periods.

acquisition of *TESS* would provide us the most unbiased coverage and confirmation of slowly rotating asteroids. However, it is still an interesting question where the cutoff of *TESS* is, above which the rotation period statistics become significantly biased. The divergence between the LCDB and *TESS* histograms starts at rotation periods of 8–10 hr. Below this period, the two statistics nicely agree down to periods of a  $\sim 2$  hr range.

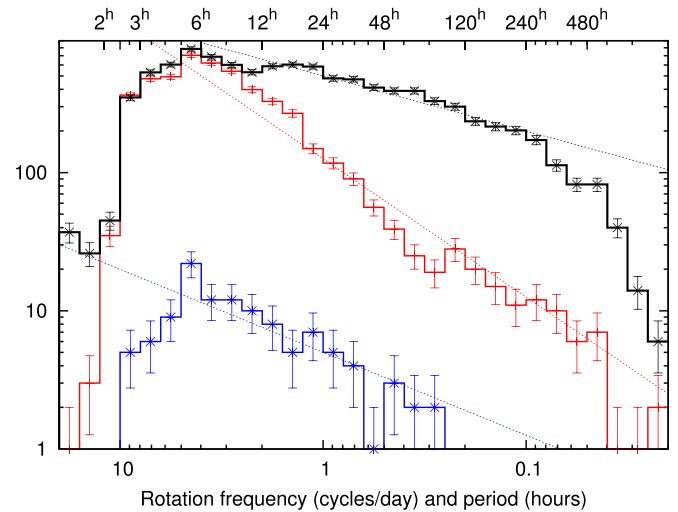


**Figure 7.** Number of objects as a function of their periods, provided by various databases. The black curve shows the period distribution for TSSYS-DR1 (9912 objects); the red curve shows the period distribution for the 4842 LCDB objects for which a valid rotation period and brightness variation amplitude have been derived at the same time. The blue curve shows the period distribution for 113 serendipitous main-belt asteroids provided by the analysis of three *K2* superstars. The thin dashed lines guide the eye to provide a tentative slope at the long-period (low-frequency) parts of these distributions.

## 6. Summary

In this paper we presented the first data release of the complete Southern Survey of the *Transiting Exoplanet Survey Satellite* in terms of analysis of bright main-belt and Trojan asteroids crossing the FoV of Camera #1. This survey triples the number of asteroids with accurately determined rotation characteristics. Another advantage of the presented catalog is that it is fully homogeneous considering both data acquisition and data processing principles. Further fine-tuning in the pipeline presented here is also possible, and we have the intention to process and add further object classes, including Centaurs, trans-Neptunian objects, and near-Earth objects (see also Milam et al. 2019).

*TESS* is now observing the northern hemisphere, opening the possibilities to reobserve many of the objects presented in this data release with a completely different observing geometry with respect to the spin-axis orientation of these bodies. Such further observations would help us to interpret the derived light-curve characteristics, specifically the amplitude in a more accurate manner and therefore helping the analysis for a more accurate comparison with LCDB. We should also express our hope that the extended mission of *TESS* would include wide coverage of the ecliptic plane, further expanding our collection of asteroid observations and increase the number of multi-epoch observations.

We would like to thank Brian D. Warner for the careful review of our paper and his highlights of many aspects of light-curve interpretation and caveats. A.P. would like to thank Matt Holman, George Ricker, Roland Vanderspek, Joel Villaseñor, and Deborah Woods for the fruitful discussions about the astrometry of *TESS* full-frame images and solar system topics in general. This paper includes data collected by the *TESS* mission. Funding for the *TESS* mission is provided by the NASA Explorer Program. This project has been supported by the Lendület Program of the Hungarian Academy of Sciences, project No. LP2018-7/2019. Additional support is received from the K-125015 and GINOP 2.3.2-15-2016-00003 grants of the National Research, Development and Innovation Office (NKFIH, Hungary). Zs.B. acknowledges the support provided from the National Research, Development and Innovation Fund of Hungary, financed under the PD<sub>17</sub> funding scheme, project No. PD-123910. L.M. was supported by the Premium Postdoctoral Research Program of the Hungarian Academy of Sciences. Cs.K. was supported by the ÚNKP-19-2 New National Excellence Program of the Ministry of Human Capacities. Partial funding of the computational infrastructure and database servers are received from the grant KEP-7/2018 of the Hungarian Academy of Sciences. Gy.M.Sz. was supported by the Hungarian NKFI grant K-119517 and the City of Szombathely under Agreement No. 67.177-21/2016. The work of G.M. was supported by the PD-128360 project of the National Research, Development and Innovation Office, Hungary. This work has made use of data from the European Space Agency (ESA) mission *Gaia*, processed by the *Gaia* Data Processing and Analysis Consortium (DPAC). Funding for the DPAC has been provided by national institutions, in particular the institutions participating in the *Gaia* Multilateral Agreement.

*Facilities:* *TESS* (Ricker et al. 2015), *Gaia* DR2 (*Gaia* Collaboration et al. 2018).

*Software:* FITSH (Pál 2012), EPHEMD.

### ORCID iDs

András Pál  <https://orcid.org/0000-0001-5449-2467>

Róbert Szakáts  <https://orcid.org/0000-0002-1698-605X>  
Csaba Kiss  <https://orcid.org/0000-0002-8722-6875>  
Attila Bódi  <https://orcid.org/0000-0002-8585-4544>  
Zsófia Bognár  <https://orcid.org/0000-0002-8493-9781>  
László L. Kiss  <https://orcid.org/0000-0002-3234-1374>  
Gábor Marton  <https://orcid.org/0000-0002-1326-1686>  
László Molnár  <https://orcid.org/0000-0002-8159-1599>  
Emese Plachy  <https://orcid.org/0000-0002-5481-3352>  
Krisztián Sárneczky  <https://orcid.org/0000-0003-0926-3950>  
Gyula M. Szabó  <https://orcid.org/0000-0002-0606-7930>  
Róbert Szabó  <https://orcid.org/0000-0002-3258-1909>

### References

- Barentsen, G., Pál, A., Sárneczky, K., & Molnár, L. 2017, *MPC*, 102428 [https://www.minorplanetcenter.net/iau/ECS/MPCArchive/2017/MPC\\_20170112.pdf](https://www.minorplanetcenter.net/iau/ECS/MPCArchive/2017/MPC_20170112.pdf)
- Benecchi, S. D., Lisse, C. M., Ryan, E. L., et al. 2018, *Icar*, 314, 265
- Borucki, W. J., Koch, D., Basri, G., et al. 2010, *Sci*, 327, 977
- Delbo, M., Mueller, M., Emery, J. P., Rozitis, B., & Capria, M. T. 2015, in *Asteroids IV*, ed. P. Michel, F. E. DeMeo, & W. F. Bottke (Tucson, AZ: Univ. Arizona Press), 107
- Farkas-Takács, A., Kiss, Cs., Pál, A., et al. 2017, *AJ*, 154, 119
- Gaia* Collaboration, Brown, A. G. A., Vallenari, A., et al. 2018, *A&A*, 616, A1
- Gaia* Collaboration, Prusti, T., de Bruijne, J. H. J., et al. 2016, *A&A*, 595, A1
- Howell, S. B., Sobek, C., Haas, M., et al. 2014, *PASP*, 126, 398
- Jordi, C., Gebran, M., Carrasco, J. M., et al. 2010, *A&A*, 523, A48
- Kiss, Cs., Marton, G., Farkas-Takács, A., et al. 2017, *ApJL*, 838, L1
- Kiss, Cs., Pál, A., Farkas-Takács, A. I., et al. 2016, *MNRAS*, 457, 2908
- Kiss, Cs., Szakáts, R., & Marton, G. 2019, *Small Bodies: Near and Far Database of Thermal Infrared Measurements of Small Solar System Bodies Public Release 1.2*, (Budapest: SBNAP) [https://ird.konkoly.hu/data/SBNAP\\_IRDB\\_public\\_release\\_note\\_2019March29.pdf](https://ird.konkoly.hu/data/SBNAP_IRDB_public_release_note_2019March29.pdf)
- Knežević, Z., & Milani, A. 2000, *CeMDA*, 78, 17
- Marciniak, A., Alí-Lagoa, V., Müller, T. G., et al. 2019, *A&A*, 625, A139
- Milam, S. N., Hammel, H. B., Bauer, J., et al. 2019, arXiv:1907.08972
- Molnár, L., Pál, A., Sárneczky, K., et al. 2018, *ApJS*, 234, 37
- Müller, T. G., Lellouch, E., Bönhardt, H., et al. 2009, *EM&P*, 105, 209
- Nesvorný, D., Brož, M., & Carruba, V. 2015, in *Asteroids IV*, ed. P. Michel, F. E. DeMeo, & W. F. Bottke (Tucson, AZ: Univ. Arizona Press), 297
- Pál, A. 2009, PhD thesis, Eötvös Loránd Univ., arXiv:0906.3486
- Pál, A. 2012, *MNRAS*, 421, 1825
- Pál, A., Kiss, Cs., Müller, Th. G., et al. 2016, *AJ*, 151, 117
- Pál, A., Molnár, L., & Kiss, Cs. 2018, *PASP*, 130, 114503
- Pál, A., Szabó, R., Szabó, Gy. M., et al. 2015, *ApJL*, 804, 45
- Pravec, P., & Harris, A. W. 2000, *Icar*, 148, 12
- Ricker, G. R., Winn, J. N., Vanderspek, R., et al. 2015, *JATIS*, 1, 014003
- Ryan, E. L., Sharkey, B. N. L., & Woodward, Ch. E. 2017, *AJ*, 153, 116
- Szabó, Gy. M., Pál, A., Kiss, Cs., et al. 2017, *A&A*, 599, A44
- Szabó, R., Pál, A., Sárneczky, K., et al. 2016, *A&A*, 596, A40
- Szabó, R., Sárneczky, K., Szabó, Gy. M., et al. 2015, *AJ*, 149, 112
- Szakáts, R., Kiss, Cs., Marton, G., et al. 2017, *EPSC*, 11, 223
- Tenenbaum, P., & Jenkins, J. M. 2018, *TESS Science Data Products Description Document, EXP-TESS-ARC-ICD-0014 Rev D*. EXP-TESS-ARC-ICD-0014 Rev D., (Baltimore, MD: STScI) <https://archive.stsci.edu/missions/tess/doc/EXP-TESS-ARC-ICD-TM-0014.pdf>
- Warner, B. D., Harris, A. W., & Pravec, P. 2009, *Icar*, 202, 134
- Zappala, V., Cellino, A., Barucci, A. M., Fulchignoni, M., & Lupishko, D. F. 1990, *A&A*, 231, 548